Materials Advances

ROYAL SOCIETY OF CHEMISTRY

PAPER

View Article Online
View Journal | View Issue

Cite this: *Mater. Adv.*, 2026, 7, 1721

Enhanced photocatalytic degradation of pollutants *via* MoS_2-integrated $DyCrO_3$ nanostructures

Md. Mahbubar Rahman, Md. Sobuj Hossain, Tasnim Jahan and M. A. Basith*

Water contamination by persistent dyes and antibiotics is a major environmental concern. Here, a $DyCrO_3$/MoS_2 S-scheme heterojunction photocatalyst was synthesized *via* a simple hydrothermal method to enhance solar-light-driven degradation efficiency. Structural and electronic analyses (XRD, FESEM, TEM, XPS, UV-vis, PL, Mott–Schottky) confirm well-dispersed MoS_2 nanosheets, oxygen vacancies, improved visible-light absorption, and favorable band alignment. MoS_2 incorporation reduced the band gap from 2.14 to 1.72 eV and prevented $DyCrO_3$ aggregation, yielding particles of 28 ± 7 to 32 ± 12 nm. The optimized $DyCrO_3$–MoS_2 (85% : 15%) composite (10 mg) degraded 84.95% of levofloxacin and 78.97% of methylene blue within 240 min, with apparent quantum yields of 37.88% and 39.59%, respectively, and strong cycle stability. Active-species trapping identified photogenerated holes as the dominant oxidants, supporting an S-scheme mechanism. These results demonstrate that MoS_2-engineered $DyCrO_3$ nanostructures provide an efficient and durable platform for solar-driven wastewater purification.

Received 8th September 2025,
Accepted 6th January 2026

DOI: 10.1039/d5ma01025j

rsc.li/materials-advances

1 Introduction

Rapid industrialization has exacerbated environmental pollution, with chemical industries-including textiles, paper, paint, and cosmetics-discharging substantial amounts of non-biodegradable chemicals, antibiotics, and hazardous dyes into aquatic systems.[1] Studies indicate that 30–90% of antibiotics enter wastewater as parent compounds or metabolites.[2] Synthetic dyes (*e.g.*, methylene blue, rhodamine B), pharmaceutical antibiotics (*e.g.*, levofloxacin, ciprofloxacin), and pesticides are now prevalent in water bodies, posing severe ecological and health risks.[3] In Bangladesh, levofloxacin concentrations have been reported up to $<$LOD-710 ng L^{-1}.[4] The complex aromatic and heterocyclic structures of these contaminants make them resistant to conventional treatments such as adsorption, reverse osmosis, chlorination, chemical oxidation, coagulation, biological degradation, and ozonolysis,[5–7] which may also generate secondary pollutants. Microbial treatments are often ineffective against bio-persistent compounds, underscoring the urgent need for advanced and efficient remediation strategies.[8]

Advanced oxidation processes (AOPs) have emerged as effective approaches for degrading persistent organic pollutants into CO_2, H_2O, and biodegradable intermediates. Among various AOPs, semiconductor-based photocatalysis has attracted considerable attention due to its ability to directly harness solar energy for the generation of highly reactive species, including superoxide ($^{\bullet}O_2^-$), hydroxyl radicals ($^{\bullet}OH$), and photogenerated holes.[9,10] In particular, visible-light-responsive semiconductors with engineered band structures and heterojunction interfaces are actively pursued to enhance solar utilization, suppress charge-carrier recombination, and improve photocatalytic stability for the efficient removal of dyes and emerging pharmaceutical contaminants.[9–12] Since visible light accounts for 43% of solar radiation, compared to 4% for UV light, visible-light-driven photocatalysts are particularly desirable.[13] While TiO_2, ZnO, and Fe_2O_3 have been extensively explored,[14–16] TiO_2's wide bandgap and rapid electron–hole recombination limit its visible-light efficiency.[17]

Rare-earth orthochromites, especially $DyCrO_3$, have emerged as promising visible-light-responsive photocatalysts.[18] $DyCrO_3$ exhibits favorable charge carrier dynamics, nanoscale particle size, tunable surface properties, oxygen vacancies, and a band-gap of 2.72 eV, which collectively enhance adsorption, charge separation, and redox activity.[19–23] However, challenges such as particle agglomeration, limited surface area, and incomplete charge separation restrict its photocatalytic potential.[24] In this study, $DyCrO_3$ nanoparticles were synthesized *via* a sol–gel method at 750 °C to investigate their photocatalytic performance.

Nanostructured transition-metal oxides (TMOs) and two-dimensional materials, particularly MoS_2, have attracted attention for photocatalytic applications due to their high surface area, layered structure, excellent electron mobility, and tunable

Nanotechnology Research Laboratory, Department of Physics, Bangladesh University of Engineering and Technology, Dhaka-1000, Bangladesh.
E-mail: mabasith@phy.buet.ac.bd

electronic properties.[25–28] Integrating $DyCrO_3$ with MoS_2 nanosheets forms an S-scheme n–n heterojunction, generating a built-in electric field that drives photogenerated electrons and holes in opposite directions, suppressing recombination and enhancing charge carrier lifetimes.[29–31] MoS_2 also prevents $DyCrO_3$ aggregation, provides abundant catalytic sites, and improves structural stability, while $DyCrO_3$ mitigates MoS_2 restacking, facilitating light penetration and charge transport. This synergy enhances reactive oxygen species formation.

Despite extensive studies on rare-earth orthochromites and two-dimensional sulfide photocatalysts, the integration of MoS_2 with $DyCrO_3$ for simultaneous dye and antibiotic degradation under solar irradiation remains underexplored. Herein, we construct a MoS_2-integrated $DyCrO_3$ S-scheme heterojunction that enhances interfacial charge separation and reactive oxygen species generation, leading to efficient visible-light-driven degradation of both methylene blue and levofloxacin. This work elucidates the structure-function correlation induced by MoS_2 incorporation and highlights MoS_2-engineered $DyCrO_3$ as an effective photocatalyst for solar wastewater remediation. $DyCrO_3$–MoS_2 nanocomposites with optimized MoS_2 loadings (5–20 wt%) were systematically developed, where both components function as n-type semiconductors with well-matched band structures that facilitate directional charge migration.[18,32,33] The S-scheme architecture exploits the layered nature of MoS_2 to increase accessible active sites, inhibit particle aggregation, and enhance recyclability. Detailed TRPL, PEC, XPS, Raman, and AQY analyses collectively establish a comprehensive structure–property–performance relationship, validating the $DyCrO_3$–MoS_2 composite as an efficient and durable photocatalyst.

2 Materials preparation and experimental techniques

2.1 Materials

The chemicals used in this study included dysprosium(III) nitrate pentahydrate ($Dy(NO_3)_3{\cdot}5H_2O$, 99.8%), chromium(III) nitrate nonahydrate ($Cr(NO_3)_3{\cdot}9H_2O$, 98.0%), citric acid ($C_6H_8O_7$, 99.5%), ammonium hydroxide (NH_4OH, 35.05 g mol^{-1}), molybdenum disulfide (MoS_2, 99% metal basis), and ethylene glycol (CH_2OH-CH_2OH, 99%). Additional reagents included levofloxacin (LFX, 98%), methylene blue (MB, 98%), isopropanol (IPA, 60.1 g mol^{-1}), ethanol (CH_3CH_2OH), acrylamide ($CH_2{=}CHCONH_2$, 99%), potassium dichromate ($K_2Cr_2O_7$, 99.8%), disodium EDTA (99.8%), *N*-methyl-2-pyrrolidone (NMP, C_5H_9NO, 99.8%), polyvinylidene fluoride (PVDF, $[CH_2CF_2]_n$, 99.8%), and sodium sulfate (Na_2SO_4, 99%). All chemicals were purchased from Sigma-Aldrich (Germany) and used without further purification.

2.2 Synthesis methods

2.2.1 Synthesis of $DyCrO_3$ nanoparticles. $DyCrO_3$ nanoparticles were prepared *via* a sol–gel method,[34] following the procedure reported in our previous study.[18] A schematic illustration of the synthesis route is provided in Fig. S1 (Route 1) in the SI.

2.2.2 Synthesis of MoS_2 nanosheets. MoS_2 nanosheets were synthesized using an ultrasonication technique,[30]as described in detail in the SI.

2.2.3 Synthesis of $DyCrO_3$–MoS_2 nanocomposites. $DyCrO_3$–MoS_2 nanocomposites were prepared *via* a facile hydrothermal method, as schematically illustrated in Fig. S1. Composites with varying MoS_2 loadings (5, 10, 15, and 20 wt%) were fabricated to optimize photocatalytic performance. For the $DyCrO_3$–MoS_2 (95% : 5%) sample, 198 mg of pre-synthesized $DyCrO_3$ nanoparticles (sol–gel method) and 22 mg of MoS_2 nanosheets were dispersed in 50 mL of a 1 : 1 (v/v) mixture of deionized water and ethanol. The suspension was magnetically stirred for 3 h to ensure homogeneity, followed by hydrothermal treatment in a Teflon-lined stainless-steel autoclave at 180 °C for 12 h. After naturally cooling to room temperature, the product was collected by centrifugation, washed repeatedly with deionized water and ethanol, and dried at 120 °C for 12 h. Nanocomposites with higher MoS_2 contents (10, 15, and 20 wt%) were synthesized using the same procedure by adjusting the MoS_2 amount accordingly.

2.3 Characterization

The crystalline structure of the synthesized materials was analyzed using X-ray diffraction (XRD) on a Rigaku SmartLab diffractometer with Cu Kα radiation (λ = 1.5406 Å). The resulting diffraction patterns were refined *via* Rietveld analysis using the FullProf Suite to extract structural parameters. Surface morphology and microstructural features were examined using field emission scanning electron microscopy (FESEM, Gemini-SEM 360, Zeiss, Germany) and transmission electron microscopy (TEM, Talos F200X, Thermo Fisher Scientific, USA). Elemental composition was determined through energy-dispersive X-ray (EDX) spectroscopy. Surface chemical states and binding energy profiles were probed using X-ray photoelectron spectroscopy (XPS, Thermo Fisher Scientific, USA). Optical properties were evaluated by UV-vis absorption spectroscopy (UV-2600, Shimadzu, Japan), while photoluminescence (PL) spectra were recorded on an RF-6000 spectrofluorophotometer (Shimadzu, Japan). Mott–Schottky (MS) measurements were performed at room temperature using a standard three-electrode setup on an electrochemical workstation (Autolab PGSTAT302N, Metrohm, Germany) to assess the semiconductor properties of the $DyCrO_3$–MoS_2 (85% : 15%) nanocomposite. The photocatalytic performance of the $DyCrO_3$–MoS_2 (85% : 15%) nanocomposite was evaluated through the degradation of methylene blue (MB) and levofloxacin (LFX) under simulated solar irradiation. A 500 W Hg–Xe arc lamp, providing a power density of 100 mW cm^{-2}, was used as the solar simulator for these studies.

2.4 Electrochemical characterization for Mott–Schottky analysis

A schematic representation of the electrode fabrication process,[35,36] and the electrochemical cell configuration employed for the Mott–Schottky measurements is provided in Fig. S2, with further procedural details outlined in the SI.

2.5 Photocatalytic characterization

A detailed discussion of the photocatalytic characterization, accompanied by the relevant schematic illustration in Fig. S3, is presented in the article in the SI.

3 Results and discussion

3.1 Structural, morphological and chemical state analysis

Rietveld-refined XRD patterns of $DyCrO_3$–MoS_2 nanocomposites with varying MoS_2 loadings are shown in Fig. 1(a)–(d), confirming the coexistence of orthorhombic $DyCrO_3$ (space group *Pnma*)[18,24,34] and hexagonal MoS_2 (space group *P*63/*mmc*).[29,30] The Rietveld-refined XRD profile of pure MoS_2 (Fig. S4, SI) exhibits sharp diffraction peaks, with the (0 0 2) reflection at 14.436° showing the highest intensity. The orthorhombic $DyCrO_3$ framework provides a stable backbone for uniform MoS_2 dispersion, while the hexagonal MoS_2 lattice facilitates ion intercalation, enhancing both structural integrity and photocatalytic performance.

Crystallite sizes of the $DyCrO_3$–MoS_2 composites with 5, 10, 15, and 20 wt% MoS_2 were calculated as 17.06, 19.28, 23.15, and 21.23 nm, respectively, using the Scherrer equation[24] (Table S1, SI). These sizes are significantly smaller than that of pure $DyCrO_3$ nanoparticles (26 nm),[18] indicating the formation of nanoscale crystallites and suggesting that MoS_2 incorporation increases the surface area.

Notably, the $DyCrO_3$–MoS_2 (85% : 15%) sample shows a shift in the (0 0 2) peak near $2\theta \approx 14°$, with an associated increase in interlayer spacing (inset of Fig. 1(b)), implying modifications in the MoS_2 interplanar distance. This peak shift likely enhances photocatalytic performance by strengthening interfacial interactions between $DyCrO_3$ and MoS_2, facilitating more efficient charge separation.

In contrast, a reduction in interlayer spacing at higher MoS_2 loadings suggests possible MoS_2 aggregation, which may hinder photocatalytic efficiency by reducing available surface area. The pronounced peak intensity at $2\theta \approx 14.19°$ further verifies the successful formation of $DyCrO_3$–MoS_2 nanocomposites across all compositions. Detailed structural parameters, including refined lattice constants and goodness-of-fit χ^2 values for both MoS_2 and $DyCrO_3$–MoS_2 systems, are presented in Table S1 in the SI.

FESEM images of $DyCrO_3$–MoS_2 nanocomposites with varying MoS_2 concentrations (Fig. 2(a)–(d)) highlight distinct morphological features. EDX spectra and particle size distributions of $DyCrO_3$–MoS_2 nanocomposites with compositions (wt%) of $DyCrO_3$ and MoS_2 are 95% : 05%, 90% : 10%, 85% : 15%, and 80% : 20%, and along with the EDX profile and sheet thickness of MoS_2 nanosheets, are illustrated in Fig. S5 in the SI. The estimated MoS_2 nanosheets thickness exhibits around 10.99 nm (Fig. S5(j), in the SI). Moreover, the particle size of $DyCrO_3$–MoS_2 (95% : 05%), $DyCrO_3$–MoS_2 (90% : 10%), $DyCrO_3$–MoS_2 (85% : 15%), and $DyCrO_3$–MoS_2 (80% : 20%) nanocomposites were found to be in the range of 28 ± 7 to 32 ± 12 nm, In comparison, $DyCrO_3$ nanoparticles range from 28 to 45 nm in size,[18] both of which play

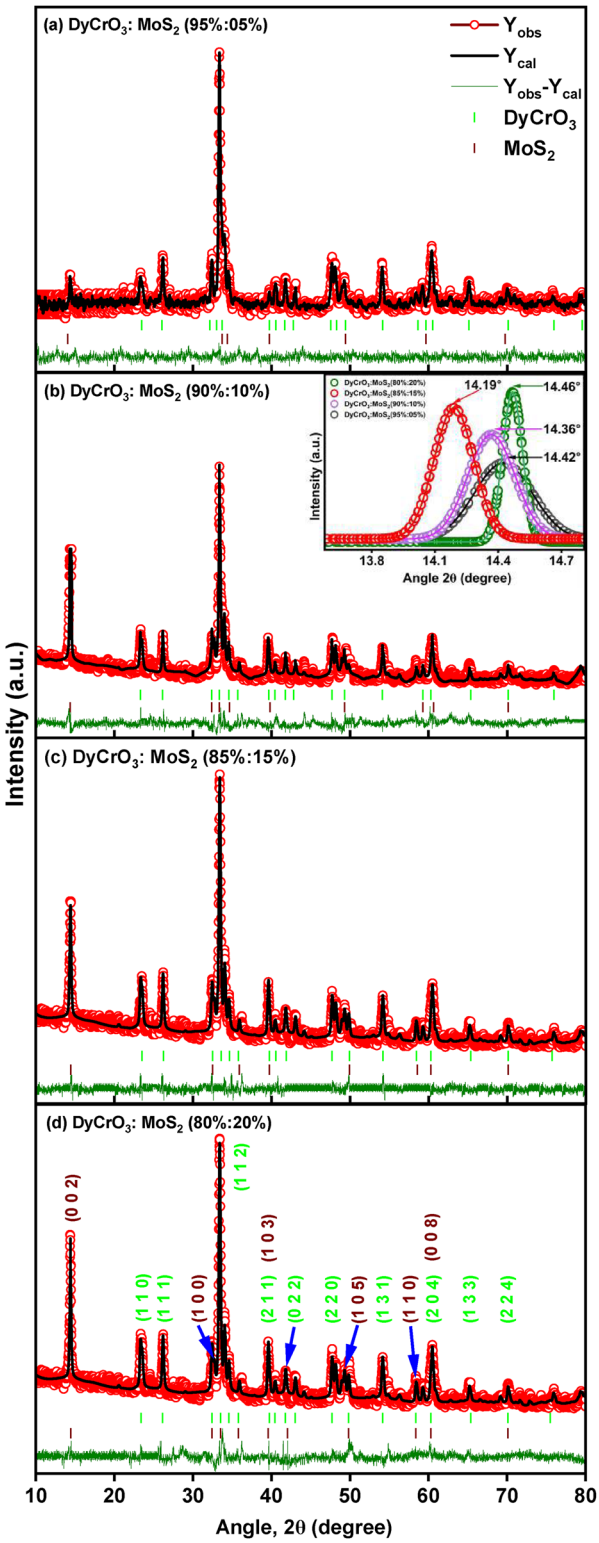

Fig. 1 Rietveld-refined XRD patterns of $DyCrO_3$–MoS_2 nanocomposites with varying MoS_2 content: (a) $DyCrO_3$–MoS_2 (95% : 5%), (b) $DyCrO_3$–MoS_2 (90% : 10%), (c) $DyCrO_3$–MoS_2 (85% : 15%), and (d) $DyCrO_3$–MoS_2 (80% : 20%). Diffraction peaks correspond to orthorhombic $DyCrO_3$ (*Pnma*) and hexagonal MoS_2 (*P*63/*mmc*), confirming phase coexistence. Inset in (b) shows a peak shift near $2\theta \approx 14.19°$, indicating changes in MoS_2 interlayer spacing, most pronounced in (c). $DyCrO_3$–MoS_2 (85% : 15%) exhibits optimal crystallinity for photocatalytic applications.

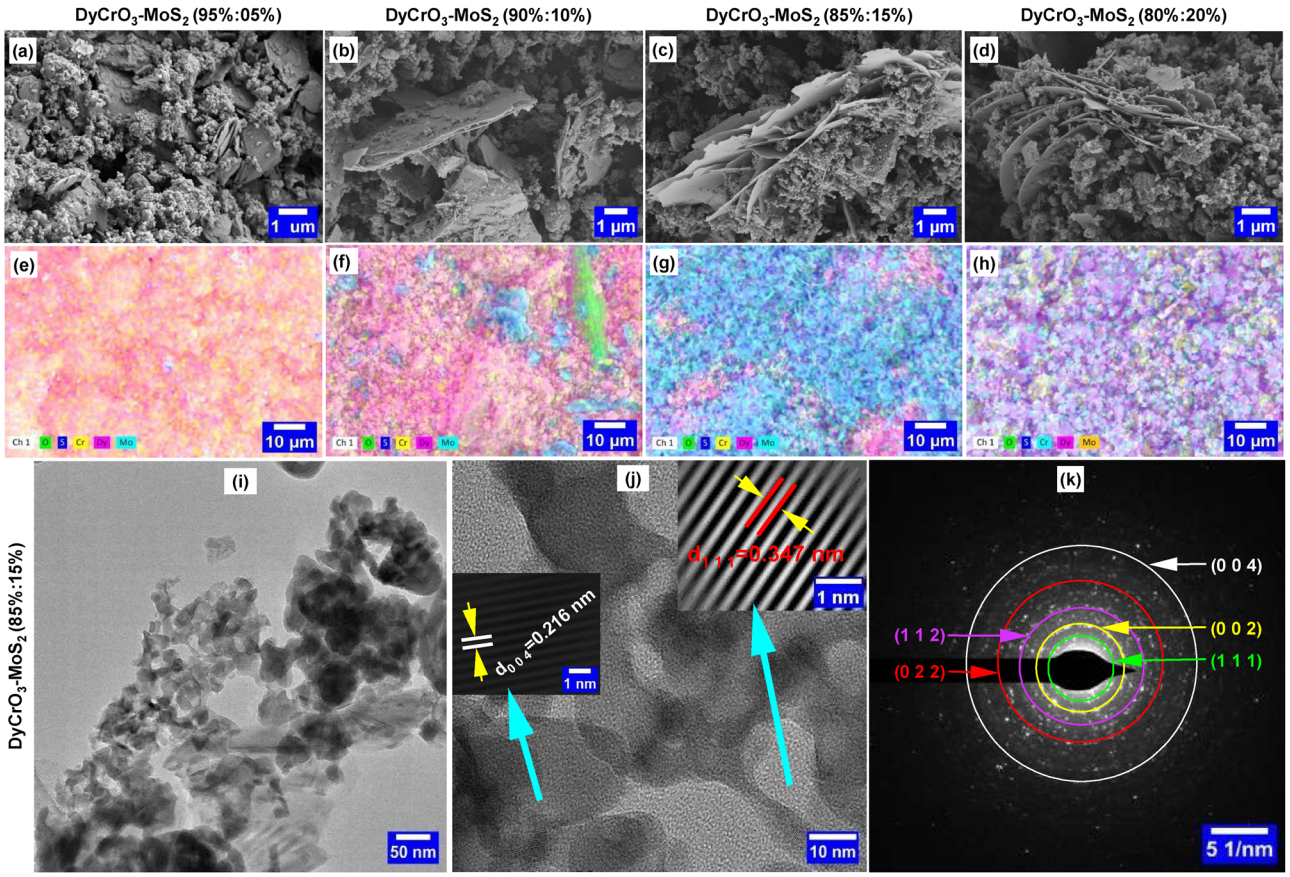

Fig. 2 Morphological characterization of $DyCrO_3$–MoS_2 nanocomposites. (a)–(d) FESEM images of $DyCrO_3$–MoS_2 (95% : 5%), $DyCrO_3$–MoS_2 (90% : 10%), $DyCrO_3$–MoS_2 (85% : 15%), and $DyCrO_3$–MoS_2 (80% : 20%) nanocomposites, showing sheet-like morphology and increased MoS_2 prominence with higher loading. (e)–(h) Corresponding elemental maps confirming uniform distribution of Dy, Cr, Mo, S, and O. (i) TEM image of $DyCrO_3$–MoS_2 (85% : 15%) composite reveals interlaced MoS_2 sheets and $DyCrO_3$ nanoparticles. (j) HRTEM shows lattice fringes indexed to $DyCrO_3$ and MoS_2. (k) SAED pattern confirms polycrystalline nature.

critical roles in influencing the composites' functionality. Moreover, mass and atomic percentages of elements in MoS_2 nanosheets, and at varying MoS_2 contents in $DyCrO_3$–MoS_2 nanocomposites were determined by EDX and theoretical analysis, which are presented in Table S2 in the SI. In the $DyCrO_3$–MoS_2 (95% : 05%) sample (Fig. 2(a)), prominent thick sheet-like morphologies indicate strong interfacial interactions between $DyCrO_3$ and MoS_2, resulting in a compact and well-integrated structure. With an increased MoS_2 content of 10% (Fig. 2(b)), more intricate sheet architectures emerge, characterized by dispersed MoS_2 clusters and reduced nanoparticle agglomeration. These features are favorable for photocatalysis, as they contribute to increased surface area, enhanced pollutant adsorption, and more efficient generation of reactive species. At the $DyCrO_3$–MoS_2 (85% : 15%) composition (Fig. 2(c)), the nanocomposite displays well-defined, larger MoS_2 sheets interlaced with $DyCrO_3$ nanoparticles, indicating strong heterointerfacial contact. In the $DyCrO_3$–MoS_2 (80% : 20%) sample (Fig. 2(d)), MoS_2 sheets appear more extensively integrated within the $DyCrO_3$ matrix, accompanied by increased sheet thickness. This may impede efficient charge transfer during photocatalytic reactions. While enhanced interfacial interactions contribute to structural integrity, the higher MoS_2 content also promotes phase separation, which can compromise compositional uniformity. These observations highlight the importance of optimizing MoS_2 loading to achieve a balance between structural coherence and photocatalytic efficiency.

Energy-dispersive X-ray spectroscopy (EDS) mapping offers further insight into the spatial distribution of elements within the $DyCrO_3$–MoS_2 nanocomposites. In the $DyCrO_3$–MoS_2 (95% : 05%) sample (Fig. 2(e)), a uniform distribution of dysprosium (Dy), chromium (Cr), and oxygen (O) confirms the integrity of the $DyCrO_3$ matrix, while the homogeneous presence of molybdenum (Mo), and sulfur (S) indicates successful MoS_2 incorporation. At 10% MoS_2 loading (Fig. 2(f)), more pronounced regions rich in Mo and S are evident, suggesting localized MoS_2 clustering. The $DyCrO_3$–MoS_2 (85% : 15%) sample (Fig. 2(g)) exhibits well-defined Mo and S domains, consistent with the presence of larger MoS_2 sheets seen in FESEM analysis. A further increase to 20% MoS_2 (Fig. 2(h)) results in intensified signals from Mo and S, confirming a higher degree of MoS_2 integration. Elemental mapping conducted for both MoS_2 nanosheets and $DyCrO_3$–MoS_2 composites (Fig. S6–S10, in the SI) validates the compositional uniformity critical for photocatalytic activity.

TEM analysis (Fig. 2(i) and (j)) further corroborates the morphology of the $DyCrO_3$–MoS_2 (85% : 15%) nanocomposite, confirming the interconnected nanocrystalline structure observed in FESEM images. While FESEM estimated particle sizes for 5, 10, 15, and 20 wt% loading of MoS_2 composites as 28.68 ± 7, 30.91 ± 12, 32.78 ± 13, and 32.40 ± 12 nm, respectively (Fig. S5 in the SI) TEM imaging (Fig. 2(i)) reveals more uniform, irregular spherical particles averaging 18 ± 10 nm in size for $DyCrO_3$–MoS_2 (85% : 15%) nanocomposite, as shown in Fig. S11. The HRTEM image (Fig. 2(j)) displays clear lattice fringes with *d*-spacing values of 0.347 nm for the (1 1 1) plane of orthorhombic $DyCrO_3$ nanoparticles and 0.216 nm for the (0 0 4) plane of hexagonal MoS_2 nanosheets, consistent with XRD results. The SAED pattern (Fig. 2(k)) exhibits prominent concentric rings, confirming the polycrystalline nature of the $DyCrO_3$–MoS_2 (85% : 15%) composite. Collectively, these morphological, elemental, and structural characterizations highlight the $DyCrO_3$–MoS_2 (85% : 15%) composition as the most structurally stable and catalytically favorable configuration, owing to its high crystallinity, uniform distribution of active sites, and enhanced interfacial integration.

X-ray photoelectron spectroscopy (XPS) analysis of the $DyCrO_3$–MoS_2 (85% : 15%) nanocomposite provides crucial insights into its surface chemistry and electronic structure. The full survey spectrum (Fig. S12(a)) confirms the presence of Dy, Cr, O, Mo, and S elements. The chemical state analysis of $DyCrO_3$–MoS_2 (85% : 15%) nanocomposite, as depicted in Fig. 3, was carried out to determine its surface composition. The formation of oxygen vacancies,[24] arising from missing oxygen atoms in the lattice, is governed by the coexistence of mixed oxidation states of transition metal ions (Cr^{2+}/Cr^{3+}) and rare-earth ions (Dy^{3+}/Dy^{4+}). In Fig. 3(a) and (b), the high-resolution Dy 4d and Dy 3d spectra reveal peaks characteristic of Dy^{4+}, and Dy^{3+}, respectively, while the Cr 2p region displays a mixture of Cr^{2+} and Cr^{3+} oxidation states (Fig. 3(c)). The Mo 3d spectrum (Fig. 3(d)) indicates the coexistence of Mo^{4+} and Mo^{6+} species, confirming the formation of Mo–S bonds, which is further supported by the S 2p (Fig. 3(e)) spectrum indicating successful sulfur incorporation from MoS_2.[29,30,37] Furthermore, the O 1s spectrum depicted in Fig. 3(f) shows a dominant contribution from oxygen vacancies, in addition to signals corresponding to metal–oxygen bonds and hydroxyl groups.[24,38–41]

Notably, the oxygen vacancy concentration in the $DyCrO_3$–MoS_2 (85% : 15%) composite (66.06%) is substantially higher than that in pristine $DyCrO_3$ nanoparticles (40%),[18] suggesting enhanced electron trapping, as depicted in Fig. 3(f). This increase in oxygen vacancies is likely to suppress charge carrier recombination, contributing to improved photocatalytic efficiency. Additionally, the presence of mixed valence states of Cr and Mo, combined with abundant oxygen vacancies, facilitates effective charge separation and promotes the formation of reactive oxygen species (ROS). These oxygen vacancies also serve as active sites for pollutant adsorption and ROS generation, further enhancing the overall photocatalytic performance of the composite.

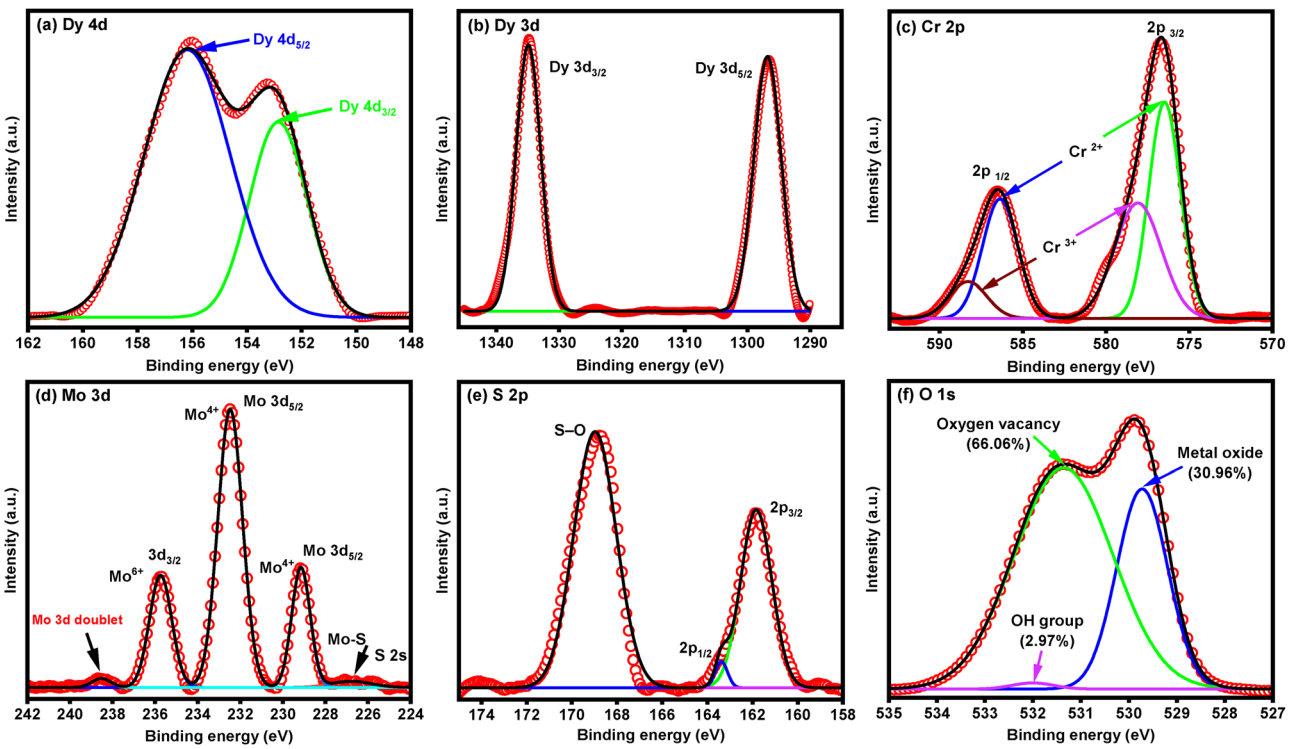

Fig. 3 XPS chemical state analysis of $DyCrO_3$–MoS_2 (85% : 15%). (a) Dy 4d, (b) Dy 3d, (c) Cr 2p, (d) Mo 3d, (e) S 2p, (f) O 1s, confirming oxidation states, successful MoS_2 incorporation, presence of oxygen vacancies, mixed-valence Cr and Mo, and Mo–S bonding, contributing to enhanced photocatalytic activity.

3.2 Optical characterization

UV-vis absorbance spectra and Tauc plots were used to estimate the optical band gaps of the $DyCrO_3$–MoS_2 nanocomposites.[42] According to the Tauc plots in Fig. 4(a)–(d), the optical band gaps for $DyCrO_3$–MoS_2 (95% : 05%), $DyCrO_3$–MoS_2 (90% : 10%), $DyCrO_3$–MoS_2 (85% : 15%), and $DyCrO_3$–MoS_2 (80% : 20%) are 2.14 eV, 2.07 eV, 1.91 eV, and 1.73 eV, respectively. With increasing MoS_2 incorporation, the band gap narrows, indicating improved visible-light absorption. Moreover, by using the Tauc model, 1.724 eV is estimated as the band gap of MoS_2 (Fig. S13). Nanocomposites' decreased band gap indicates that MoS_2 insertion successfully alters the electrical band structure, promoting better charge separation and transfer.

Steady-state photoluminescence (PL) spectra of $DyCrO_3$–MoS_2 nanocomposites with varying MoS_2 content are shown in Fig. 4, providing insights into charge carrier dynamics and optical properties. Emission peaks corresponding to optical band gaps of 2.14 eV, 1.94 eV, 1.85 eV, and 1.69 eV are observed in the PL spectra presented in Fig. 4(e)–(h), recorded at an excitation wavelength of 220 nm for $DyCrO_3$–MoS_2 (95% : 05%), $DyCrO_3$–MoS_2 (90% : 10%), $DyCrO_3$–MoS_2 (85% : 15%), and $DyCrO_3$–MoS_2 (80% : 20%), respectively. The redshift in PL emission peaks and the reduced band gap with increasing MoS_2 content indicate enhanced solar light absorption. These results suggest that a 15 wt% MoS_2 content is optimal for improving the photocatalytic activity of $DyCrO_3$–MoS_2 nanocomposites.

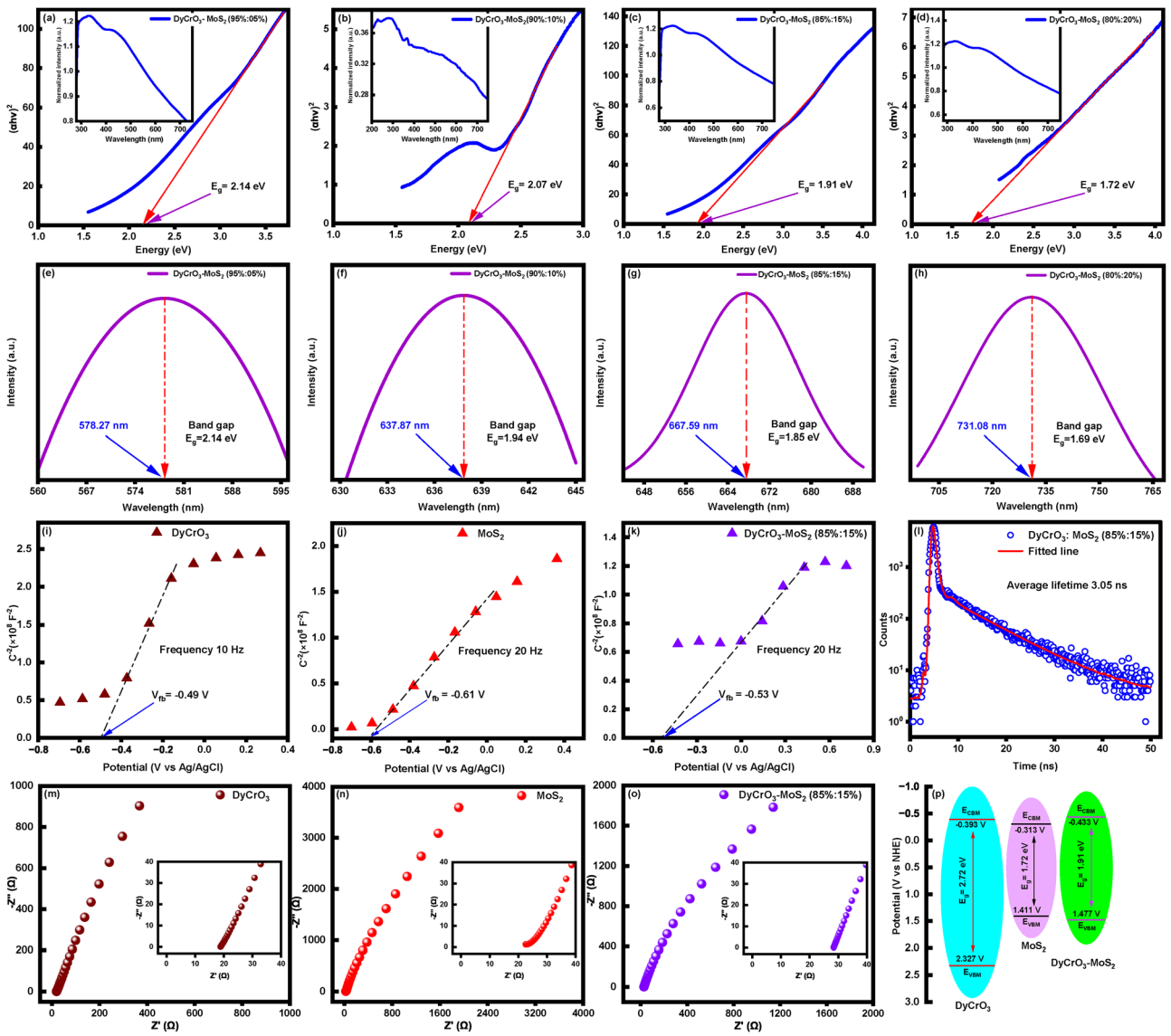

Fig. 4 Optical and electronic characterization of $DyCrO_3$–MoS_2 nanocomposites. (a)–(d) Tauc plots of $DyCrO_3$–MoS_2 (95% : 5%), $DyCrO_3$–MoS_2 (90% : 10%), $DyCrO_3$–MoS_2 (85% : 15%), and $DyCrO_3$–MoS_2 (80% : 20%) samples; insets show UV-vis absorbance. Band gap narrows with increasing MoS_2. (e)–(h) PL spectra (λ_{ex} = 220 nm) confirm band gap reduction (2.14–1.69 eV). (i)–(k) Mott–Schottky plots indicate n-type behavior. (l) TRPL decay of $DyCrO_3$–MoS_2 (85% : 15%) showing an average lifetime of 3.05 ns, evidencing suppressed recombination. (m) and (n) show the electrochemical impedance spectroscopy (EIS) results. (o) $DyCrO_3$–MoS_2 (85% : 15%) nanocomposite. (p) Band alignment schematic illustrates favorable positions for ROS generation.

The Mott–Schottky plots in Fig. 4(i)–(k) verify the n-type semiconducting behavior of $DyCrO_3$–MoS_2 nanocomposites,[24,43,44] with flat band potentials (V_{fb}) of −0.49 V, −0.61 V, and −0.53 V (*vs.* Ag/AgCl) for $DyCrO_3$, MoS_2, and $DyCrO_3$–MoS_2 (85% : 15%), respectively. XPS analysis revealed that the valence band of the 15 wt% MoS_2-loaded composite *i.e.*, $DyCrO_3$–MoS_2 (85% : 15%) is positioned at 1.54 V (Fig. 10(g)). Using the optical band gap values in combination with the V_{fb} measurements, the calculated band edge positions as discussed in details in the SI, were illustrated in Fig. 4(p), giving VBM/CBM values of 2.327 V/−0.393 V, 1.411 V/−0.313 V, and 1.477 V/−0.433 V (*vs.* NHE) for $DyCrO_3$, MoS_2, and $DyCrO_3$–MoS_2 (85% : 15%), respectively.

To further verify the charge-carrier recombination dynamics, time-resolved photoluminescence (TRPL) measurements were performed for the $DyCrO_3$–MoS_2 (85% : 15%) nanocomposite under 375 nm pulsed excitation. The decay curve (Fig. 4(l)) was fitted using a bi-exponential function, yielding an average lifetime of approximately 3.05 ns. The prolonged lifetime compared to typical oxide-based photocatalysts indicates efficient separation and slower recombination of photogenerated charge carriers across the $DyCrO_3$/MoS_2 interface.[24] This result aligns well with the steady-state PL quenching and the reduced charge-transfer resistance observed from EIS, confirming the superior photoinduced charge-separation efficiency of the $DyCrO_3$–MoS_2.

The more negative CBM values enhance the thermodynamic driving force for the reduction of oxygen to $^{\bullet}O_2^-$, a key ROS in organic pollutant degradation. Similarly, the positive VBM values facilitate water oxidation to $^{\bullet}OH$, another potent ROS, thereby supporting efficient photocatalysis. In addition, the electrochemical impedance spectroscopy (EIS) results, illustrated in Fig. 4(m)–(o) for $DyCrO_3$ nanoparticles, MoS_2 nanosheets, and $DyCrO_3$–MoS_2 (85% : 15%) nanocomposite, reveal the absence of arc radii in the insets of Fig. 4(m)–(o), indicating minimal charge transfer resistance. This reflects efficient charge carrier separation and suppressed electron–hole recombination[45,46] contributing to the improved photocatalytic performance.

3.3 Photoelectrochemical analysis

Photoelectrochemical (PEC) investigations were performed to elucidate the interfacial charge-transfer behaviour of the $DyCrO_3$–MoS_2 (85% : 15%) nanocomposite under dark and illuminated conditions (Fig. 5). The linear sweep voltammetry (LSV) curves (Fig. 5a) reveal a pronounced enhancement in current density upon illumination, increasing from 3.6 A g^{-1} in the dark to 9.9 A g^{-1} at 2.8 V under simulated solar light. This more than twofold increase in photocurrent directly confirms the efficient generation and separation of photoinduced charge carriers within the $DyCrO_3$/MoS_2 heterojunction. The superior photocurrent response under illumination originates from the S-scheme charge-transfer pathway that drives spatially separated redox reactions across the interface. The cyclic voltammetry (CV) profiles (Fig. 5b) recorded at a scan rate of 100 mV s^{-1} further substantiate this behaviour, displaying a substantially larger enclosed area under light irradiation compared with the dark condition. The enlarged CV loop implies higher capacitive response, improved interfacial redox kinetics, and enhanced reversibility of charge storage processes triggered by photoexcitation. Electrochemical impedance spectroscopy (EIS) measurements (Fig. 5c) complement these findings. The Nyquist plots exhibit a markedly smaller semicircle radius under illumination, indicating a lower charge-transfer resistance (R_{ct}) and faster interfacial electron migration. The inset highlights the high-frequency region, where the slope increase signifies improved ionic/electronic conductivity and reduced recombination probability. Collectively, the LSV, CV, and EIS analyses confirm that $DyCrO_3$–MoS_2 (85% : 15%) demonstrates superior photoelectrochemical activity under visible-light excitation due to efficient interfacial charge separation and accelerated surface redox dynamics, thereby substantiating its outstanding photocatalytic performance.

3.4 Evaluation of photocatalytic performance

The solar-driven photocatalytic performance of $DyCrO_3$–MoS_2 nanocomposites was evaluated using two representative water pollutants: LFX, a colorless antibiotic, and MB, a colored dye.

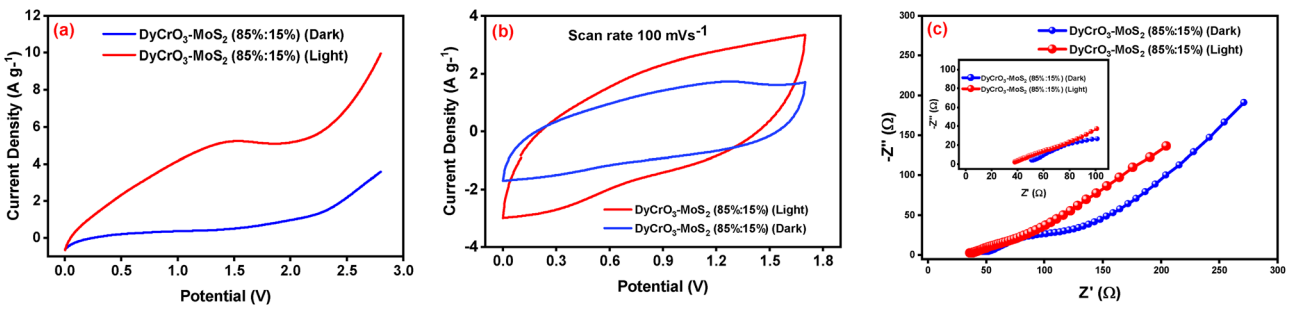

Fig. 5 Photoelectrochemical (PEC) characteristics of $DyCrO_3$–MoS_2 (85% : 15%) nanocomposite under dark and illuminated conditions in 1 M Na_2SO_4 electrolyte using a two-electrode configuration. (a) Linear sweep voltammetry (LSV) curves exhibiting a pronounced enhancement in photocurrent density under illumination, confirming efficient photo-induced charge separation. (b) Cyclic-voltammetry (CV) profiles recorded at a scan rate of 100 mV s^{-1} showing an enlarged enclosed area under light exposure, indicative of improved interfacial redox kinetics and electrochemical reversibility. (c) Nyquist plots from electrochemical impedance spectroscopy (EIS) revealing a smaller semicircle radius under illumination, signifying reduced charge-transfer resistance and accelerated carrier transport.

While LFX exhibited substantial degradation under sunlight, MB showed an even more pronounced response, highlighting the influence of pollutant optical properties on photocatalytic activity. This comparative approach allowed for a comprehensive investigation of photocatalytic behavior under different optical conditions.

Fig. 6(a) presents the photocatalytic degradation efficiency of LFX as a function of $DyCrO_3$–MoS_2 (80% : 20%) nanocomposite dosage under solar irradiation. The corresponding absorbance spectra for various dosages (5, 10, 20, and 40 mg) are shown in Fig. S14, in the SI. Initially, increasing the catalyst dosage enhanced the degradation rate due to the greater availability of active sites, which improved light absorption and facilitated the generation of reactive oxygen species (ROS), including $OH^{\bullet}$ and $^{\bullet}O_2^-$. The degradation efficiency peaked at 10 mg, while further increases in dosage led to a plateau at 20 mg and a notable decline at 40 mg. This decrease is attributed to excessive particle loading, causing agglomeration and reduced light penetration, thereby lowering photocatalytic activity. Consequently, 10 mg was identified as the optimal dosage, balancing active surface area with effective light utilization.

Similar trends were observed for both LFX (Fig. 6(b)) and MB (Fig. 6(c)) across different MoS_2 loadings. Lower MoS_2 contents (5, and 10 wt%) resulted in reduced degradation efficiency, likely due to insufficient active sites and less effective ROS generation. Conversely, excessive MoS_2 incorporation (20 wt%) negatively impacted activity, presumably due to increased nanosheet thickness and agglomeration, which limited light penetration and decreased accessible surface area, hindering ROS formation. The degradation efficiency of LFX and MB under solar irradiation at the optimized 10 mg dosage for different MoS_2 loadings is shown in Fig. S15 and S16, respectively. Pseudo-first-order kinetic analysis for LFX degradation with varying $DyCrO_3$–MoS_2 (80% : 20%) dosages (Fig. 6(d)) revealed the highest rate constant of 0.01154 min^{-1} at 10 mg.

Using this optimized 10 mg dosage, $DyCrO_3$–MoS_2 nanocomposites with varying MoS_2 concentrations were tested for LFX and MB degradation. Both pollutants exhibited increased reaction rate constants with higher MoS_2 content. Notably, the $DyCrO_3$–MoS_2 (85% : 15%) composition demonstrated the highest pseudo-first-order rate constants: 0.01416 min^{-1} for LFX (Fig. 6(e)) and 0.00829 min^{-1} for MB (Fig. 6(f)), reflecting the optimal balance of active surface area and light absorption. Based on these results, the 10 mg dosage of the $DyCrO_3$–MoS_2 (85% : 15%) nanocomposite was selected for all subsequent photocatalytic studies to ensure consistent and efficient performance.

The corresponding UV-vis absorption spectra (Fig. 7(a) and (b)) show a progressive decline in peak intensity accompanied by a hypochromic shift over time, confirming the effective photocatalytic degradation of LFX and MB by the $DyCrO_3$–MoS_2 (85% : 15%) nanocomposite.[43,47] These results underscore the photocatalytic competence of the nanocomposite under

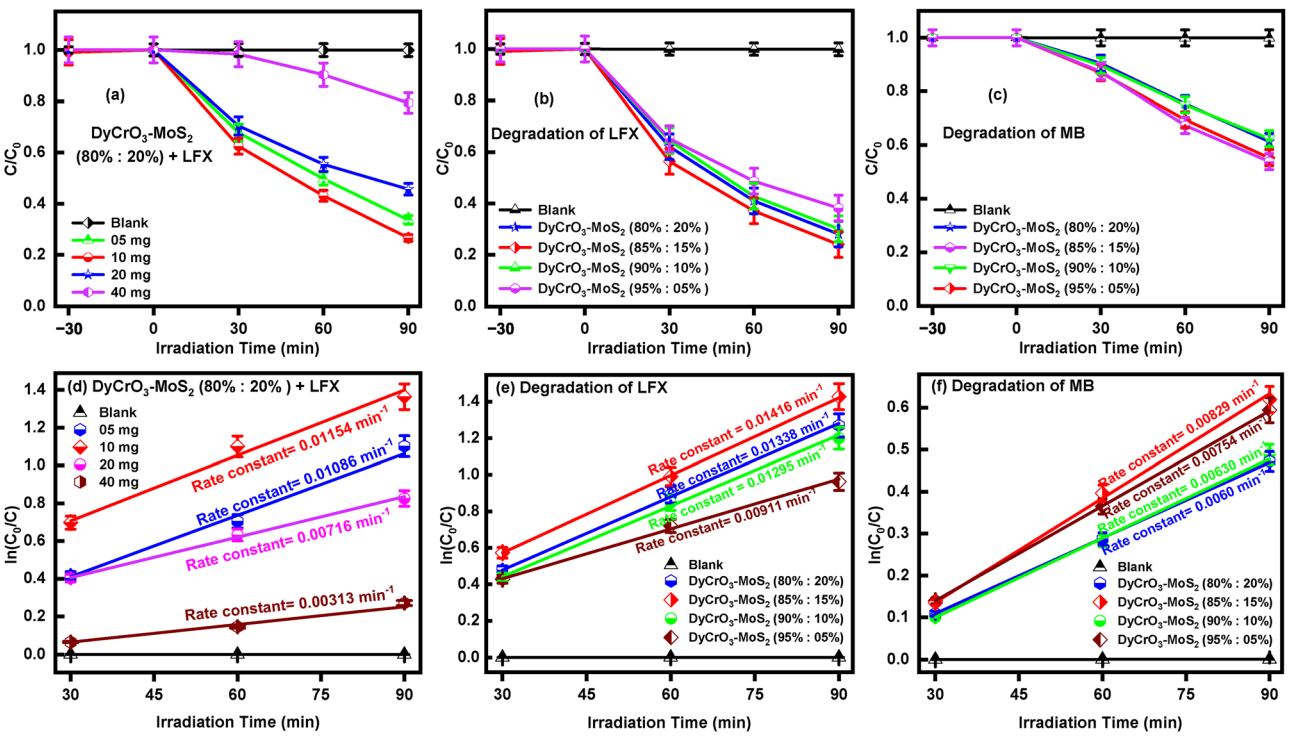

Fig. 6 Photocatalytic performance of $DyCrO_3$–MoS_2 nanocomposites. (a) Effect of $DyCrO_3$–MoS_2 (80% : 20%) catalyst dosage (5, 10, 20, 40 mg) on LFX degradation. (b) and (c) Degradation efficiencies of LFX and MB after 90 min under 500 W Hg–Xe lamp for 5–20% MoS_2, showing enhanced activity. (d)–(f) Pseudo-first-order kinetics, confirming increased reaction rates with higher MoS_2 loading.

simulated solar irradiation. The degradation efficiency was quantitatively determined using the following expression.[18,24]

$$\text{Photocatalytic degradation } (\%) = \left(\frac{C_0 - C}{C_0}\right) \times 100$$

where C_0 and C represent the initial and time-dependent concentrations of the pollutants, respectively. Among the studied samples, the $DyCrO_3$–MoS_2 (85% : 15%) nanocomposite exhibited superior photocatalytic activity. After 240 minutes of irradiation with a 500 W Hg–Xe lamp, the $DyCrO_3$–MoS_2 (85% : 15%) nanocomposite exhibited degradation efficiencies of 84.95% for LFX and 79.87% for MB, highlighting its superior photocatalytic performance (Fig. 7(c)). The catalyst also showed an efficient degradation of CIP (68.51%) under identical conditions (Fig. S17). Pseudo-first-order kinetic analyses for LFX (0.00794 min^{-1}) and MB (0.00606 min^{-1}) degradation revealed markedly higher reaction rates with the $DyCrO_3$–MoS_2 (85% : 15%) nanocomposite than the control samples, confirming its efficacy for removing pharmaceutical and dye pollutants from wastewater (Fig. 7(d)). These results highlight the synergistic enhancement in photocatalytic performance attributed to the incorporation of MoS_2.

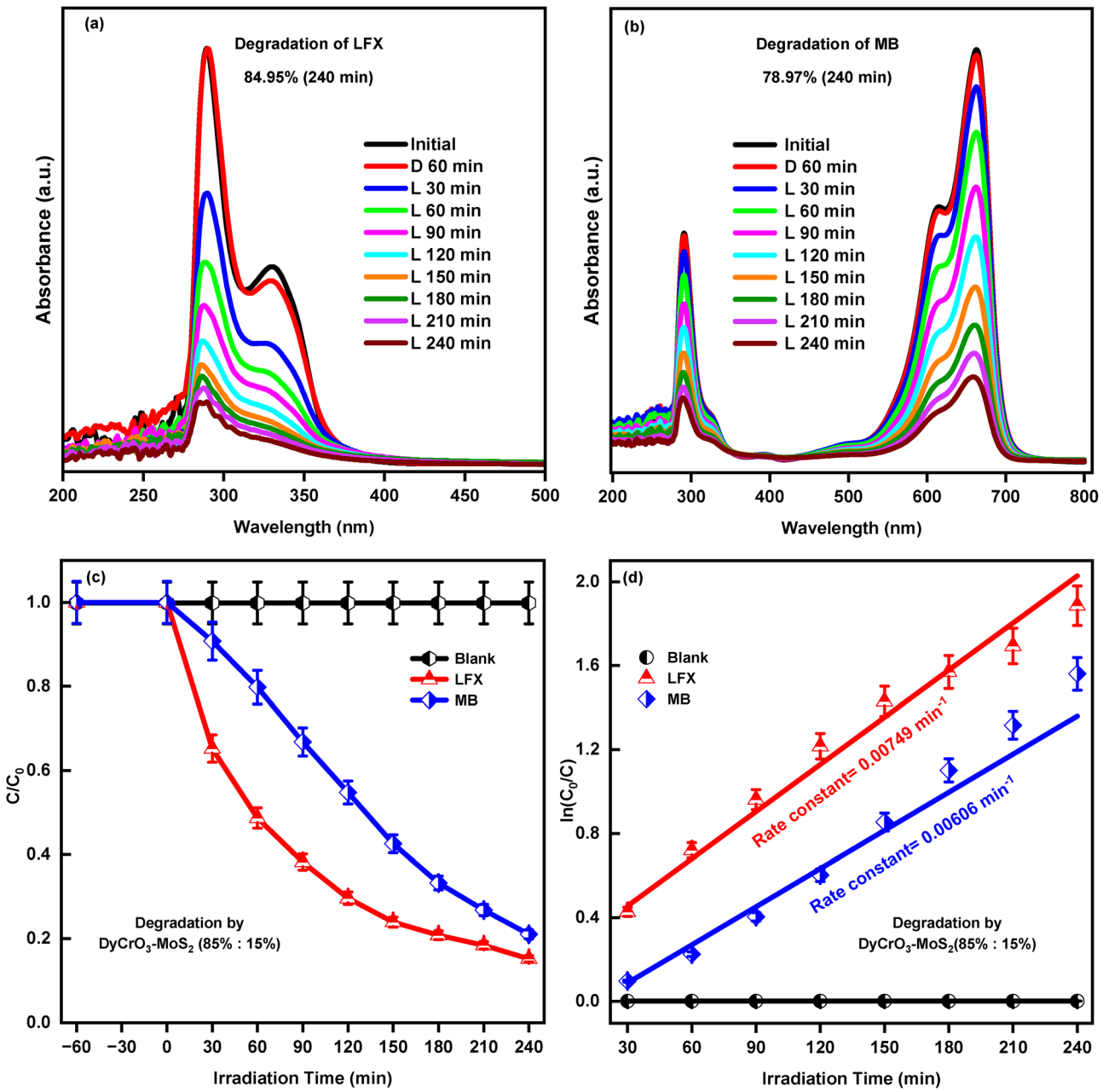

Fig. 7 Photocatalytic degradation of LFX and MB using $DyCrO_3$–MoS_2 (85% : 15%). (a) and (b) UV-vis spectra showing time-dependent degradation of LFX and MB. (c) Degradation efficiencies for 240 min: 84.95% (LFX), 79.87% (MB). (d) Pseudo-first-order kinetics indicate enhanced reaction rates compared to controls.

Notably, the $DyCrO_3$–MoS_2 (85% : 15%) nanocomposites demonstrated significantly higher photocatalytic activity than pristine $DyCrO_3$ nanoparticles, which achieved only 70% MB degradation under identical conditions.[18] This enhancement emphasizes the critical role of MoS_2 in promoting charge separation and extending light absorption, thereby improving overall photocatalytic performance. Interestingly, during the first 120 minutes, LFX degradation (70%) was approximately 25% higher than that of MB (45%), highlighting the influence of pollutant optical properties and reaction kinetics. These results collectively underscore the $DyCrO_3$–MoS_2 (85% : 15%) nanocomposite as the most structurally and catalytically favorable composition for solar-driven pollutant degradation.

To further elucidate the degradation mechanism, kinetic studies were performed using a pseudo-first-order model. The experimental data were fitted according to the following expression:[18,24,48]

$$\ln\left(\frac{C_0}{C}\right) = kt$$

where, k is the reaction rate constant and t is the irradiation time, enabling a quantitative comparison of degradation kinetics. The corresponding kinetic plots are presented in Fig. 6(d)–(f). For LFX degradation using 10 mg of $DyCrO_3$–MoS_2 (80% : 20%), the highest rate constant of 0.01154 min^{-1} was obtained (Fig. 6(d)). Notably, the same optimized dosage of $DyCrO_3$–MoS_2 (85% : 15%) exhibited even higher rate constants of 0.01416 min^{-1} for LFX (Fig. 6(e)) and 0.00829 min^{-1} for MB (Fig. 6(f)). In contrast, pristine $DyCrO_3$ nanoparticles showed a significantly lower rate constant of 0.00472 min^{-1} for MB degradation,[18] indicating that MoS_2 incorporation more than doubled the photocatalytic efficiency.

Our composite shows an apparent rate constant of 0.00606 min^{-1} for methylene blue (MB, 12 mg L^{-1}) and 0.00794 min^{-1} for levofloxacin (LFX, 10 mg L^{-1}) using only 10 mg catalyst (0.1 g L^{-1}) under a 500 W Hg–Xe lamp for 240 min, achieving ~80–85% degradation efficiency. In comparison, bulk MoS_2 (20 mg, sunlight, 240 min) shows 63% degradation with $k = 3.5 \times 10^{-3}$ min^{-1},[49] layered MoS_2 nanosheets (20 mg, 150 W visible lamp, 120 min) exhibit $k = 7.7 \times 10^{-3}$ min^{-1} (oxidative) and 81.7×10^{-3} min^{-1} (reductive),[50] while a ZnS:CdS mixture (50 mg, 500 W halogen lamp, 360 min) records $k = 3.61 \times 10^{-3}$ min^{-1}.[51] Despite employing 2–5 times less catalyst, the $DyCrO_3$–MoS_2 composite demonstrates comparable or better kinetics and significantly broader pollutant applicability. Importantly, most MoS_2- and ZnS-based systems focus solely on dye degradation, whereas our study extends to LFX, a non-chromophoric antibiotic resistant to photosensitized oxidation. Achieving high degradation of both dye and antibiotic pollutants under identical visible-light conditions highlights the robustness and universality of the $DyCrO_3$–MoS_2 photocatalyst.

The superior performance of the $DyCrO_3$–MoS_2 (85% : 15%) nanocomposite can be attributed to a synergistic combination of factors. The 15 wt% MoS_2 loading provides an optimal balance between active catalytic sites and effective light penetration, while simultaneously enhancing charge carrier separation through efficient electron transfer pathways. This minimizes electron–hole recombination, promoting the generation of reactive oxygen species (ROS) that drive pollutant degradation. Although the $DyCrO_3$–MoS_2 (80% : 20%) sample exhibits a slightly narrower band gap, this advantage is offset by reduced light accessibility and potential recombination effects, making the $DyCrO_3$–MoS_2 (85% : 15%) composition the most efficient overall.

3.4.1 Activation energy calculation. To assess the efficiency and practical potential of photocatalysts in wastewater treatment, it is essential to determine the activation energy (E_a) associated with the degradation of target pollutants. Activation energy represents the minimum energy required for a chemical reaction to occur,[52,53] and a lower (E_a) indicates that the photocatalytic process can proceed more readily under the given conditions, reflecting greater energy efficiency. Evaluating (E_a) provides critical insight into the intrinsic properties of the photocatalyst, particularly its ability to harness solar energy and generate reactive species responsible for pollutant breakdown. Furthermore, comparing activation energies obtained in the presence and absence of the photocatalyst allows a quantitative assessment of its influence on reaction kinetics, highlighting its role in lowering the energy barrier and enhancing overall degradation rates.

To further evaluate the catalytic potential, the activation energy (E_a) for LFX degradation was determined using the Arrhenius equation:[24,54]

$$\ln(k) = \ln(A) - \frac{E_a}{RT}$$

where R is the universal gas constant (J mol^{-1} K^{-1}), T is the absolute temperature (K), and A is the pre-exponential factor. The activation energy was calculated from the slope of the $\ln k$ *vs.* $1/T$ curve. Fig. 8 illustrates the temperature-dependent degradation of LFX. In the absence of a photocatalyst (Fig. 8(a)), the rate constants at 10, 30, and 50 °C are 0.0022, 0.00622, and 0.01188 min^{-1}, respectively, reflecting a thermally activated process. With the $DyCrO_3$–MoS_2 (85% : 15%) nanocomposite (Fig. 8(b)), the corresponding rate constants increase to 0.0039, 0.0076, and 0.0123 min^{-1}, indicating a substantial acceleration of the degradation process.

The Arrhenius plots (Fig. 8(c)) reveal that E_a decreases from 30.03 ± 3.87 kJ mol^{-1} (without photocatalyst) to 21.49 ± 1.05 kJ mol^{-1} in the presence of $DyCrO_3$–MoS_2 (85% : 15%), confirming the enhanced photocatalytic performance of the nanocomposite. For comparison, pristine $DyCrO_3$ exhibits an E_a of 20.85 kJ mol^{-1}.[18] The slightly higher activation energy for the composite is still indicative of efficient catalysis and arises from the synergistic interplay between $DyCrO_3$ and MoS_2. This synergy improves solar light absorption, promotes charge separation, and enhances ROS generation, collectively contributing to superior photocatalytic degradation.

Overall, the $DyCrO_3$–MoS_2 (85% : 15%) nanocomposite demonstrates strong potential as a highly efficient, solar-

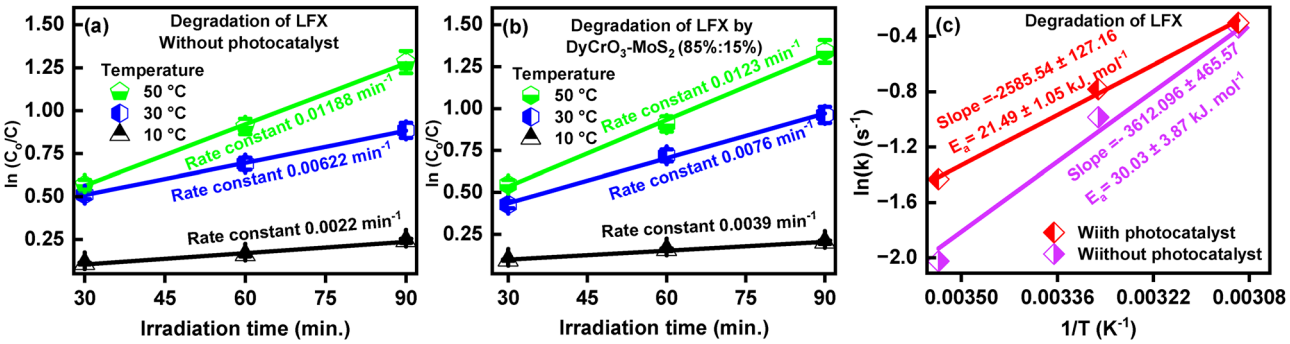

Fig. 8 Temperature-dependent degradation kinetics and activation energy analysis for LFX. (a) Kinetic plots without photocatalyst at 10, 30, 50 °C. (b) Corresponding plots with $DyCrO_3$–MoS_2 (85% : 15%), showing substantially increased rates. (c) Arrhenius plots indicate a marked reduction in activation energy with the nanocomposite, confirming improved thermal kinetics and catalytic efficiency.

driven photocatalyst, suitable for sustainable wastewater treatment and environmental remediation.

3.4.2 Apparent quantum yield (AQY). The apparent quantum yield (AQY) is a key metric for evaluating photocatalytic efficiency, as it quantitatively measures the fraction of incident photons that are successfully converted into chemical transformations, such as the degradation of pollutants. A higher AQY indicates more effective utilization of solar energy, underscoring the photocatalyst's potential for sustainable wastewater treatment. The AQY values for the nanocomposites, provided in detail in the SI, were calculated using the following expression:[18,55,56]

$$\text{AQY}\ (\%) = \frac{\text{Number of degraded molecules}}{\text{Number of incident photons}} \times 100$$

Fig. 9(a) illustrates that the $DyCrO_3$–MoS_2 (85% : 15%) nanocomposite exhibited the highest apparent quantum yield (AQY) values after the first photocatalytic cycle, achieving 37.88% for LFX, 39.59% for MB, and 36.21% for CIP. In contrast, after seven consecutive degradation cycles, the AQY values slightly decreased to 35.37%, 36.68%, and 34.76% for LFX, MB, and CIP, respectively, indicating excellent photocatalytic stability and reusability. The minor decline in AQY may be attributed to partial catalyst surface fouling or slight loss during recovery, rather than structural degradation. These results suggest that this composition offers an optimal synergy between charge separation efficiency, visible-light absorption, and active surface reactivity. Furthermore, this composition demonstrated inferior AQY performance, underscoring the pivotal role of MoS_2 content in enhancing photon-to-chemical energy conversion. Overall, these findings confirm that the $DyCrO_3$–MoS_2 (85% : 15%) nanocomposite functions as a highly efficient, durable, and recyclable solar-driven photocatalyst, particularly effective for the degradation of organic pollutants such as MB, LFX, and CIP, making it a promising candidate for sustainable wastewater purification.

3.4.3 Active species trapping experiments. Active species trapping experiments were conducted to identify the reactive species involved in LFX degradation (Fig. 9(b)). In the absence of scavengers, the highest degradation efficiency was observed. The addition of acrylamide ($^{\bullet}O_2^-$ scavenger), silver nitrate (electron scavenger), EDTA-2Na (hole scavenger), and isopropanol ($OH^{\bullet}$ scavenger) led to noticeable decreases in efficiency, confirming the involvement of these species. The most significant reduction occurred with EDTA-2Na, indicating that

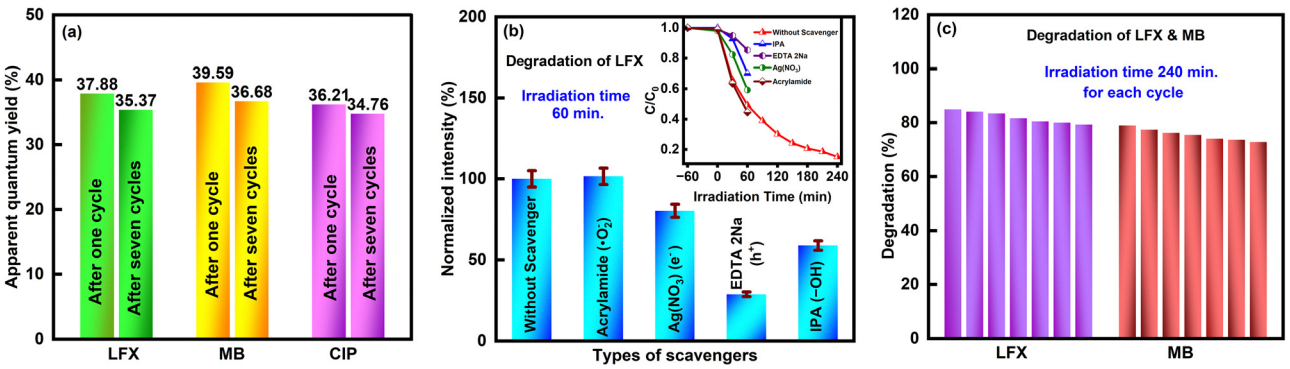

Fig. 9 Photocatalytic efficiency and mechanistic insights. (a) AQY of $DyCrO_3$–MoS_2 (85% : 15%) nanocomposite: 37.88% (LFX), 39.59% (MB), and CIP (36.21%), indicating superior efficiency before seven cycles of pollutants degradation. (b) Reactive species trapping for LFX identifies photogenerated holes as dominant species, with $^{\bullet}O_2^-$, electrons, and $OH^{\bullet}$ also contributing. (c) Reusability tests over seven cycles show minimal efficiency loss for both LFX and MB.

photogenerated holes (h^+) are the dominant reactive species. These results suggest that the $DyCrO_3$–MoS_2 (85% : 15%) nanocomposite possesses favorable band edge positions that promote efficient charge separation and facilitate the formation of $OH^\bullet$ and $^\bullet O_2^-$ radicals, thereby enhancing overall photocatalytic performance.

3.4.4 Reusability and post-cycle characterizations. Reusability studies are essential for evaluating the long-term stability and practical applicability of photocatalysts. An efficient photocatalyst should maintain high degradation efficiency over multiple cycles, thereby reducing operational costs and minimizing environmental impact. Fig. 9(c) illustrates the degradation efficiencies of LFX and MB before and after seven consecutive photocatalytic cycles using $DyCrO_3$–MoS_2 nanocomposites with varying MoS_2 content. To emphasize the tested compositions, the $DyCrO_3$–MoS_2 (85% : 15%) nanocomposite demonstrated excellent reusability, retaining approximately 79.27% and 72.79% of its initial degradation efficiency for both LFX and MB after seven cycles, respectively. This minimal reduction in activity highlights the catalyst's robust structural and chemical stability under repeated solar irradiation, confirming its durability and reinforcing its potential for real-world wastewater treatment applications. The negligible decline in activity emphasizes the resilience of the photocatalyst, making it a strong candidate for scalable and sustainable environmental remediation strategies.

To further elucidate the structural integrity and durability of the nanocomposite, post-cycle characterization was conducted. Rietveld refinement of XRD patterns for the $DyCrO_3$–MoS_2 (85% : 15%) nanocomposite before and after seven photocatalytic cycles is shown in Fig. 10(a) and (b). The crystal structure remains largely unaltered, with crystallite sizes of 22.88 nm before cycling and 21.98 nm after seven cycles (SI Table S1). Preservation of crystallinity is crucial for maintaining steady photocatalytic performance, as structural changes could disrupt active sites and hinder intercomponent interactions.

FESEM images (Fig. 10(c) and (d)) further confirm the morphological stability of the nanocomposite. The MoS_2 nanosheets retain their sheet-like morphology, while $DyCrO_3$ nanoparticles exhibit only minor agglomeration and a slight increase in sheet thickness after four cycles. This morphological preservation ensures that active sites remain accessible, sustaining high photocatalytic activity over repeated use.

Surface chemical states were evaluated using XPS. Survey spectra (Fig. S12(a)) confirm the presence of Dy, Cr, Mo, S, and O before and after seven cycles, demonstrating no elemental loss. Dy 4d and Dy 3d spectra (Fig. S12(b) and (c)) display unchanged binding energies and peak symmetry, verifying the stability of Dy^{3+} and Dy–O coordination. The O 1s spectra (Fig. 10(e) and (f)) show nearly identical lattice-oxygen, oxygen-vacancy, and hydroxyl components, with the vacancy fraction decreasing only slightly from 69.06% to 66.36%, indicating preservation of defect sites essential for charge separation and ROS generation. In the Cr 2p region (Fig. S12(d)), Cr^{3+} and minor Cr^{2+} species remain present, with a small increase in Cr^{2+} after cycling, suggesting mild surface reduction that may support interfacial charge compensation. The Mo 3d spectrum (Fig. S12(e) and (f)) shows significant evolution in the Mo 3d and S 2p regions. The Mo 3d spectrum (Fig. S12(e)) of the fresh catalyst exhibits a well-defined Mo 3d doublet associated with Mo^{6+} (Mo $3d_{5/2}$ at 235.75 eV) and Mo^{4+} (232.44 and 229.13 eV) contributions. However, after seven photocatalytic cycles, the characteristic Mo 3d doublet almost completely disappears, and the region collapses. This pronounced loss of the doublet may be attributed to the extensive $Mo^{6+} \rightarrow Mo^{4+}$ reduction and the generation of defect-associated Mo–S active sites through redox-driven surface reconstruction.[57] A comparable transformation is observed in the S 2p spectrum (Fig. S12(f)), where the well-resolved S^{2-} doublet present in the pristine sample is significantly suppressed after cycling; notably, the S $2p_{1/2}$ peak effectively disappears, and the remaining S 2p signal broadens with an enhanced S–O contribution. This behaviour signifies the formation of sulfur vacancies and mild surface oxidation during sustained photocatalysis, while the persistence of the S $2p_{3/2}$ component confirms that the MoS_2 lattice framework remains largely intact. Such defect generation is widely recognized to facilitate interfacial charge transport and contributes to the excellent catalytic durability of the composite. Electronic and vibrational stability were further examined using VB-XPS and Raman spectroscopy. The VB-XPS spectra (Fig. 10(g)) show an unchanged valence-band maximum at $\sim$1.54 eV after seven cycles, confirming preservation of electronic structure and band alignment. Raman spectra (Fig. 10(h)) maintain all characteristic $DyCrO_3$ modes (Dy–O bending, Cr–O stretching, octahedral vibrations[58,59]) and MoS_2 bands (E^1_{2g} at $\sim$383 cm^{-1}, A_{1g} at $\sim$408 cm^{-1} (ref. 60 and 61)) with negligible intensity variation, indicating no structural degradation or phase change. FTIR spectra (Fig. 10(i)) show minimal differences before and after photocatalysis, with characteristic S–S stretching at 959 cm^{-1},[62] Mo–S vibrations near 600 cm^{-1},[63,64] Cr–O stretching at 524 cm^{-1}, and Dy^{3+}-related phonon modes near 445 cm^{-1} (ref. 18) preserved. The peak at $\sim$571.83 cm^{-1} remains consistent with MoS_2 signatures.[65]

Collectively, the XRD, FESEM, XPS, VB-XPS, Raman, and FTIR results confirm that $DyCrO_3$–MoS_2 (85% : 15%) maintains its crystal structure, morphology, surface chemistry, electronic configuration, and vibrational framework during repeated cycling, demonstrating outstanding durability and suitability for long-term photocatalytic applications.

3.4.5 Photocatalysis mechanism. The enhanced photocatalytic activity of the $DyCrO_3$–MoS_2 (85% : 15%) nanocomposite is attributed to an S-scheme heterojunction mechanism under visible-light irradiation (Fig. 11 and 12). Both $DyCrO_3$ and MoS_2 are n-type semiconductors, with the conduction band (CB) of $DyCrO_3$ (−0.393 V, Fig. 4(p)) more negative than that of MoS_2 (−0.313 V, Fig. 4(p)), as determined *via* Tauc plots (Fig. 8(b) of our previous report,[18] S13) and Mott–Schottky analyses (Fig. 4(i) and (j)). When the two semiconductors form a heterojunction, electrons transfer from $DyCrO_3$ (reduction photocatalyst, RP) to MoS_2 (oxidation photocatalyst, OP), creating an internal electric field directed from $DyCrO_3$ to MoS_2 (Fig. 11(c)).

This interfacial electric field, together with Fermi-level alignment and Coulombic interactions (Fig. 11(a) and (b)), induces

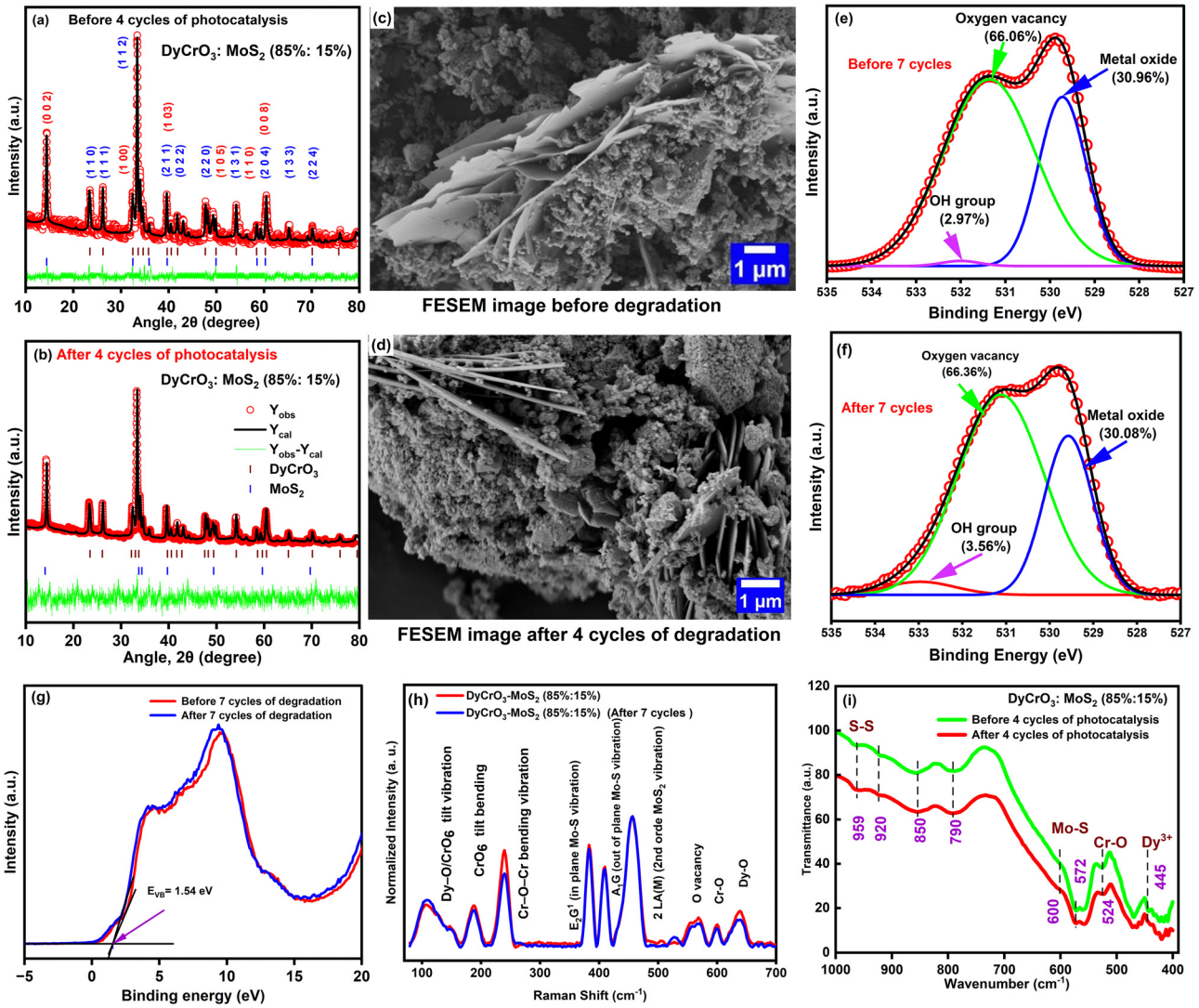

Fig. 10 Post-photocatalytic stability of $DyCrO_3$–MoS_2 (85 : 15). (a) and (b) XRD patterns before and after seven cycles showing preserved crystal structure. (c) and (d) FESEM images indicating retained nanosheet morphology. (e) and (f) O 1s XPS spectra confirming nearly unchanged oxygen-vacancy and metal-oxide components. (g) VB-XPS showing an unchanged valence-band maximum after seven cycles. (h) Raman spectra with all $DyCrO_3$ and MoS_2 modes maintained. (i) FTIR spectra before and after cycling showing minimal variation. These results confirm excellent structural, chemical, and electronic stability during repeated photocatalysis.

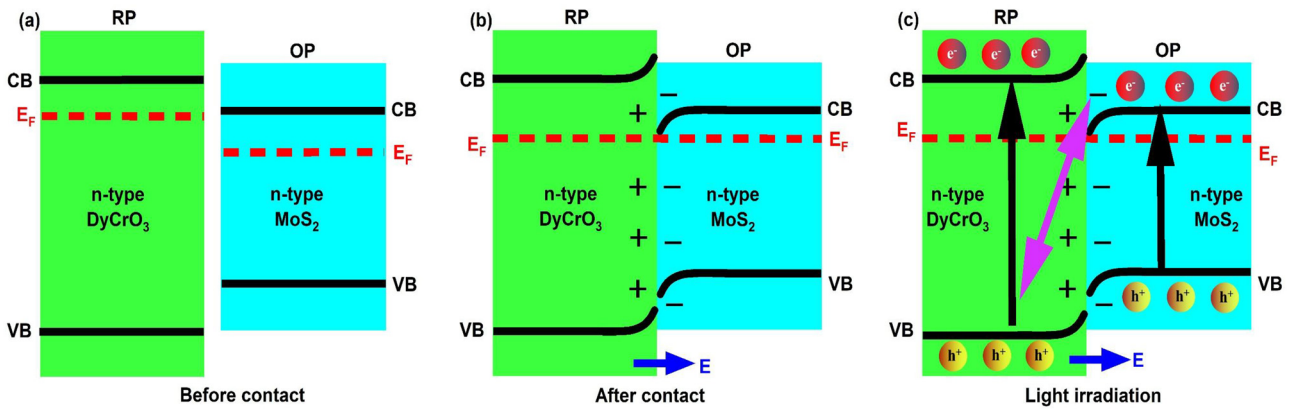

Fig. 11 Charge-transfer mechanism in the S-scheme heterojunction. (a)–(c) Schematic illustrating staggered band alignment: (a) before contact, (b) after interfacial contact, (c) photoinduced charge-carrier migration under illumination.

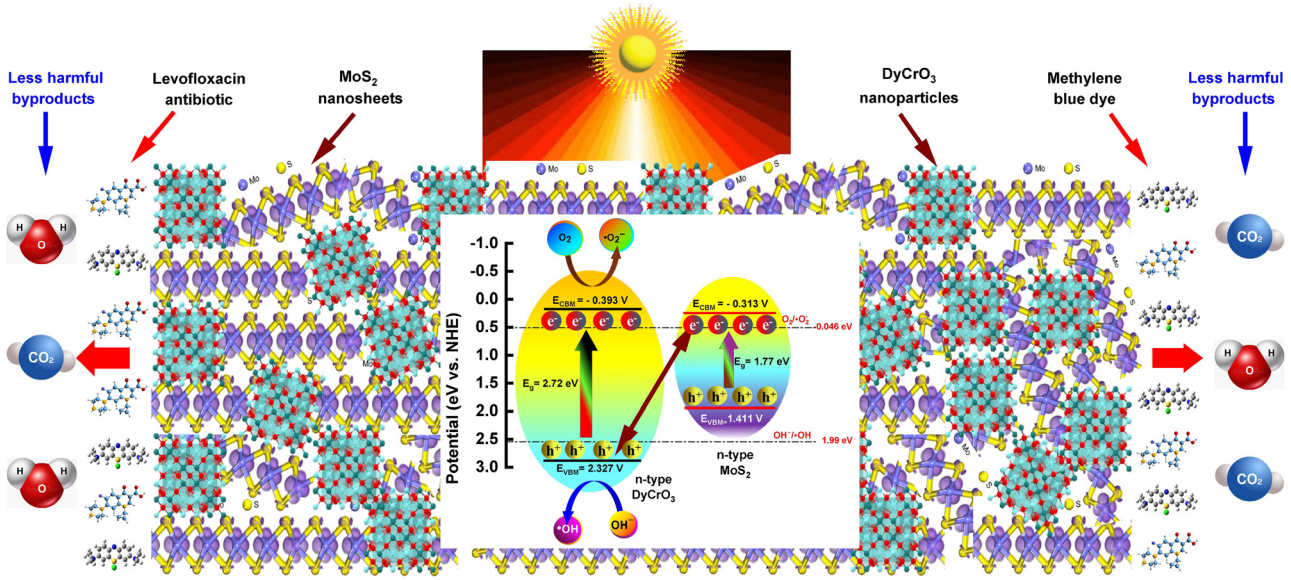

Fig. 12 Photocatalytic degradation pathway of LFX and MB. Schematic of $DyCrO_3$–MoS_2 (85% : 15%) nanocomposite under solar light. Photon absorption by $DyCrO_3$ generates electron–hole pairs; electrons transfer to MoS_2, enhancing charge separation and ROS formation ($^{\bullet}O_2^-$, $OH^{\bullet}$) to decompose LFX and MB into intermediates, ultimately converting to CO_2, H_2O, and inorganic ions.

band bending and selective recombination of low-energy carriers. Specifically, CB electrons of MoS_2 recombine with VB holes of $DyCrO_3$ at the interface (Fig. 11(c)), while high-energy electrons in $DyCrO_3$ CB and holes in MoS_2 VB are preserved. It should be noted that charge separation in the $DyCrO_3$–MoS_2 S-scheme heterojunction is governed by interfacial band bending and the built-in electric field rather than direct long-range valence-band-to-valence-band hole transfer. These charge carriers drive the generation of reactive oxygen species (ROS), such as $^{\bullet}O_2^-$ and $OH^{\bullet}$, responsible for the photocatalytic degradation of LFX and MB (Fig. 7 and 11).

In addition to heterojunction formation, oxygen vacancies in $DyCrO_3$ (Fig. 11) play a critical role in enhancing photocatalytic performance. These vacancies act as electron-capturing centers, improving charge separation and facilitating ROS generation. Adsorbed oxygen reacts with electrons at these vacancies to form $^{\bullet}O_2^-$ radicals, while holes oxidize water or hydroxyl ions to produce $OH^{\bullet}$ radicals. MoS_2 nanosheets contribute further by providing abundant active sites for pollutant adsorption and promoting interfacial electron transfer, which suppresses electron–hole recombination. The photocatalytic degradation process can be summarized as:

$$DyCrO_3/MoS_2 + h\nu \rightarrow e^-_{CB,DyCrO_3} + h^+_{VB,DyCrO_3}$$

$$e^-_{CB,DyCrO_3} + O_2 \rightarrow {}^{\bullet}O_2^-$$

$${}^{\bullet}O_2^- + 2HO_2 \rightarrow e^-_{CB,DyCrO_3} + 2OH^{\bullet} + 2OH^-$$

$$h^+ + \text{pollutants} \rightarrow \text{byproducts}$$

$$OH^{\bullet} + \text{pollutants} \rightarrow \text{byproducts}$$

Consequently, the combined effects of oxygen vacancies in $DyCrO_3$ and the structural and electronic features of MoS_2 result in efficient charge separation, enhanced ROS generation, and improved adsorption, collectively driving the high photocatalytic activity of the nanocomposite. The S-scheme architecture, optimized $DyCrO_3$–MoS_2 (85% : 15%), and 10 mg dosage ensure maximal light absorption, interfacial charge transfer, and active-site availability, making the $DyCrO_3$–MoS_2 nanocomposite highly effective for solar-driven environmental remediation (Fig. 10 and 11). Overall, the integration of MoS_2 with $DyCrO_3$ offers several advantages for visible-light photocatalysis. The formation of an S-scheme heterojunction significantly enhances charge separation and suppresses electron–hole recombination, leading to higher degradation efficiency compared to pristine $DyCrO_3$. The optimized $DyCrO_3$–MoS_2 (85% : 15%) nanocomposite also benefits from improved surface activity and stability. However, the photocatalytic performance depends on the MoS_2 loading ratio, as excessive MoS_2 may induce light-shielding effects, highlighting the importance of compositional optimization.

4 Conclusions

A $DyCrO_3$/MoS_2 S-scheme heterojunction photocatalyst was synthesized *via* a simple hydrothermal approach and thoroughly characterized. The S-scheme interface established a strong internal electric field that enhanced charge separation and reactive oxygen species generation. The optimized $DyCrO_3$–MoS_2 (85% : 15%) nanocomposite achieved 84.95% degradation of levofloxacin and 78.97% degradation of methylene blue within 240 min under visible light. TRPL, PEC, band-edge

analysis, and radical-trapping experiments confirmed efficient carrier utilization and improved light harvesting, resulting in superior kinetics and quantum yield. Post-cycling XPS and Raman analyses verified excellent structural stability and reusability. Overall, the $DyCrO_3$–MoS_2 heterostructure demonstrates strong potential as a durable and efficient solar-driven photocatalyst for wastewater purification. Future work may expand its applicability to a broader range of emerging pollutants.

Author contributions

Md. Mahbubar Rahman: investigation; methodology; visualization; writing – original draft. Md. Sobuj Hossain: investigation; writing – review & editing. Tasnim Jahan: investigation; writing – review & editing. M. A. Basith: conceptualization; resources; funding acquisition; validation; supervision; writing – review & editing.

Conflicts of interest

There are no conflicts to declare.

Data availability

The data supporting this article have been included as part of the supplementary information (SI). Supplementary information: experimental method; UV absorption spectra of LFX and MB; apparent quantum yield (AQY) calculation; comparative photocatalytic performance of $DyCrO_3$ with other perovskite oxide; activation energy experiment; Rietveld refinement XRD patterns of $DyCrO_3$ nanoparticle pre and post cycle photocatalysis. In this study, $DyCrO_3$/MoS_2 S-scheme nanostructures were synthesized by integrating $DyCrO_3$ nanoparticles (an n-type semiconductor) with MoS_2 nanosheets (an n-type semiconductor). See DOI: https://doi.org/10.1039/d5ma01025j.

Acknowledgements

We sincerely acknowledge the Committee for Advanced Studies and Research (CASR) at the Bangladesh University of Engineering and Technology (BUET), which has been instrumental in the successful execution of this research.

Notes and references

1 M. Sakamoto, T. Ahmed, S. Begum and H. Huq, *Sustainability*, 2019, **11**, 1951.
2 H. Gao, J. Angadi, S. Wang, X. Zhou, H. Yang, A. M. Al-Enizi, M. Ubaidullah, B. Pandit, D. Li and M. Gupta, *Adv. Sustainable Syst.*, 2024, **8**, 2300533.
3 R. Shanmuganathan, M. S. Kadri, T. Mathimani, Q. H. Le and A. Pugazhendhi, *Chemosphere*, 2023, **332**, 138812.
4 U. Salma, Y. Nishimura, M. Tokumura, A. Hossain, K. Watanabe, K. Noro, M. Raknuzzaman, T. Amagai and M. Makino, *Chemosphere*, 2025, **370**, 143956.
5 S. Gupta, Y. Mittal, R. Panja, K. B. Prajapati and A. K. Yadav, in *Current Developments in Biotechnology and Bioengineering*, ed. S. Kumar, R. Kumar and A. Pandey, Elsevier, 2021, pp. 47–75.
6 P. V. Messina and P. C. Schulz, *J. Colloid Interface Sci.*, 2006, **299**, 305–320.
7 S. Muthupoongodi, T. Linda, X. S. Shajan, L. Mitu and S. Balakumar, *Polym. Bull.*, 2018, **75**, 1867–1893.
8 P. N. Egbuikwem, G. C. Obiechefu, F. I. Hai, M. C. E. Devanadera and D. P. Saroj, *Environ. Technol. Rev.*, 2021, **10**, 77–110.
9 J. S. Chang, Y. W. Phuan, M. N. Chong and J. D. Ocon, *J. Ind. Eng. Chem.*, 2020, **83**, 303–314.
10 R. Gade, J. Ahemed, K. L. Yanapu, S. Y. Abate, Y.-T. Tao and S. Pola, *J. Environ. Chem. Eng.*, 2018, **6**, 4504–4513.
11 M. Subburu, R. Gade, V. Guguloth, P. Chetti, K. R. Ravulapelly and S. Pola, *J. Photochem. Photobiol., A*, 2021, **406**, 112996.
12 K. Masula, Y. Bhongiri, G. R. Rao, P. V. Kumar, S. Pola and M. Basude, *Opt. Mater.*, 2022, **126**, 112201.
13 M. Pirhashemi and A. Habibi-Yangjeh, *Ceram. Int.*, 2015, **41**, 14383–14393.
14 Q. Guo, C. Zhou, Z. Ma and X. Yang, *J. Adv. Mater.*, 2019, **31**, 1901997.
15 A. Mclaren, T. Valdes-Solis, G. Li and S. C. Tsang, *J. Am. Chem. Soc.*, 2009, **131**, 12540–12541.
16 C. Hitam and A. Jalil, *J. Environ. Manage.*, 2020, **258**, 110050.
17 J. A. Rengifo-Herrera and C. Pulgarin, *J. Chem. Eng.*, 2023, 146875.
18 M. M. Rahman, F. Yasmeen, M. Tarek and M. Basith, *J. Alloys Compd.*, 2025, **1010**, 177295.
19 Y. F. Abed, S. Das, M. S. Ali, Z. Rana and M. A. Basith, *Mater. Lett.*, 2022, **318**, 132159.
20 M. Rani, S. Dahiya and N. Panwar, *Ceram. Int.*, 2022, **48**, 19925–19936.
21 Q. Ji, L. Bi, J. Zhang, H. Cao and X. S. Zhao, *Energy Environ. Sci.*, 2020, **13**, 1408–1428.
22 M. Periyasamy, S. Sain, U. Sengupta, M. Mandal, S. Mukhopadhyay and A. Kar, *Mater. Adv.*, 2021, **2**, 4843–4858.
23 H. Xiao, P. Liu, W. Wang, R. Ran, W. Zhou and Z. Shao, *Energy Fuels*, 2020, **34**, 9208–9221.
24 M. Tarek, F. Yasmeen and M. A. Basith, *J. Mater. Chem. A*, 2024, **12**, 25475–25490.
25 U. Chinnathambi, R. Chandrapal, R. Aiswarya, B. Palanivel and T. Kalaivani, *J. Cluster Sci.*, 2025, **36**, 43.
26 X. Yang, L. Wen, H. Huang, Y. Wang, L. Wei and J. Yang, *Solid State Sci.*, 2022, **133**, 107014.
27 X. Qiu, T. Zhang, Z. Dai, R. Cao and T. Wei, *Ionics*, 2022, **28**, 939–949.
28 R. Mohammed, M. E. M. Ali, E. Gomaa and M. Mohsen, *Environ. Nanotechnol. Monit. Manage.*, 2023, **19**, 100772.
29 A. M. Tama, S. Das, S. Dutta, M. Bhuyan, M. Islam and M. A. Basith, *RSC Adv.*, 2019, **9**, 40357–40367.
30 M. Tarek and M. A. Basith, *J. Mater. Chem. C*, 2023, **11**, 16605–16622.

31 Q. Chen, J.-L. Li, Q.-L. Mo and F.-X. Xiao, *Chem. Eng. J.*, 2024, **497**, 154584.
32 R. Kumari and R. Kumar, *ECS J. Solid State Sci. Technol.*, 2023, **12**, 097004.
33 H. Khan, A. Mehtab, J. Ahmed, S. E. Lofland, K. V. Ramanujachary and T. Ahmad, *ChemNanoMat*, 2023, **9**, e202300091.
34 M. Tarek, F. Yasmeen and M. A. Basith, *Nanoscale*, 2025, **17**, 6620–6636.
35 M. Islam, M. Tarek, M. A. Adib and M. A. Basith, *J. Phys. D: Appl. Phys.*, 2024, **57**, 215302.
36 F. Yasmeen, M. Tarek and M. A. Basith, *ACS Appl. Mater. Interfaces*, 2024, **16**, 47535–47550.
37 S. Hasan, A. H. Reaz, S. Das, C. K. Roy and M. A. Basith, *J. Mater. Chem. C*, 2022, **10**, 7980–7996.
38 M. Islam, M. Tarek, R. Rashid, M. Bally, F. Ara and M. A. Basith, *Mater. Adv.*, 2025, **6**, 1379–1391.
39 D.-Q. Yang and E. Sacher, *J. Phys. Chem. C*, 2009, **113**, 6418–6425.
40 R. Liu, Z. Wang, S. Peng, J. Bi, J. Wu and Z.-G. Ye, *J. Am. Ceram. Soc.*, 2020, **103**, 1097–1104.
41 S. Jain, J. Shah, N. S. Negi, C. Sharma and R. K. Kotnala, *Int. J. Energy Res.*, 2019, **43**, 4743–4755.
42 P. Makuła, M. Pacia and W. Macyk, *How to correctly determine the band gap energy of modified semiconductor photocatalysts based on UV-Vis spectra*, 2018.
43 M. A. Adib, F. Sharmin and M. A. Basith, *Nanoscale Adv.*, 2023, **5**, 6194–6209.
44 M. Hosen, M. Tarek, M. Bhuyan, M. A. Basith and I. Syed, *Nanoscale Adv.*, 2025, **7**, 1742–1753.
45 T. Xiong, H. Wang, Y. Zhou, Y. Sun, W. Cen, H. Huang, Y. Zhang and F. Dong, *Nanoscale*, 2018, **10**, 8066–8074.
46 Y. Li, L. Ding, Y. Guo, Z. Liang, H. Cui and J. Tian, *ACS Appl. Mater. Interfaces*, 2019, **11**, 41440–41447.
47 M. S. Ali, S. Das, Y. F. Abed and M. A. Basith, *Phys. Chem. Chem. Phys.*, 2021, **23**, 22184–22198.
48 V. Ramar and K. Balasubramanian, *ACS Appl. Nano Mater.*, 2021, **4**, 5512–5521.
49 N. Chaudhary, P. Yadav and V. Bisht, *AIP Conf. Proc.*, 2020, **2276**, 020030.
50 J. Kisała, R. Wojnarowska-Nowak and Y. Bobitski, *Sci. Rep.*, 2023, **13**, 14148.
51 N. Soltani, E. Saion, M. Z. Abdul Hamid and A. Rezaee Khadangi, *Int. J. Mol. Sci.*, 2012, **13**, 12242–12258.
52 E. Muetterties, *Science*, 1977, **196**, 839–848.
53 O. Christensen, A. Bagger and J. Rossmeisl, *ACS Catal.*, 2024, **14**, 2151–2161.
54 J. Velázquez, R. Fernández-González, L. Daz, E. P. Melián, V. Rodrguez and P. Núñez, *J. Alloys Compd.*, 2017, **721**, 405–410.
55 M. J. Muñoz-Batista, A. Kubacka and M. Fernández-Garca, *Catal. Sci. Technol.*, 2014, **4**, 2006–2015.
56 J. Barrio, D. Mateo, J. Albero, H. Garca and M. Shalom, *Adv. Energy Mater.*, 2019, **9**, 1902738.
57 X. Zhang, X. Zhang, Y. Liu, X. Li, Y. Wang, Y. Zhao and H. Huang, *Appl. Catal., B*, 2020, **263**, 118358.
58 M. C. Weber, J. Kreisel, P. A. Thomas, M. Newton, K. Sardar and R. I. Walton, *Phys. Rev. B: Condens. Matter Mater. Phys.*, 2012, **85**, 054303.
59 L. Li, F. Chen, J.-Q. Lu and M.-F. Luo, *J. Phys. Chem. A*, 2011, **115**, 7972–7977.
60 S. Cortijo-Campos, P. Kung, C. Prieto and A. de Andres, *J. Phys. Chem. C*, 2021, **125**, 23904–23910.
61 T. Livneh and J. E. Spanier, *2D Mater.*, 2015, **2**, 035003.
62 K. R. Mamaghani and N. Parvin, *J. Mater. Sci.*, 2023, **58**, 12182–12201.
63 R. Leelavathi, K. Vivekanandan and V. Hariharan, *Acta Phys. Pol., A*, 2024, **145**, 361–369.
64 A. Kaur, S. Rana, A. Bharti, G. R. Chaudhary and N. Prabhakar, *Microchim. Acta*, 2021, **188**, 222.
65 S. Ahmad, I. Khan, A. Husain, A. Khan and A. M. Asiri, *Polymers*, 2020, **12**, 3047.